Enhancing Strength and Toughness of Adhesive Joints via Micro-Structured Mechanical Interlocking

Alex Hamilton[1], Yang Xu[1*], Mehmet E. Kartal[2], Nikolaj Gadegaard[1] and Daniel M. Mulvihill[1*]

[1]James Watt School of Engineering, University of Glasgow, Glasgow, G12 8QQ, UK
[2]School of Engineering, University of Aberdeen, Aberdeen, AB24 3UE, UK

ABSTRACT

The potential to improve the mechanical properties of adhesive joints via micro-structured interlocking features is investigated. The micro-structured surfaces were fabricated in polycarbonate via injection moulding from a master template. The specimens were then bonded in an interlocking configuration to form single lap joints and tested to failure in tension. Planar untreated (i.e. un-abraded) and planar roughened (i.e. abraded) samples were also tested to provide benchmarks. Compared to the planar roughened case, results show that micro-structuring the interface can yield up to a 95.9% increase in strength and up to 162% increase in work to failure. Increases in strength and work to failure beyond the planar roughened level are attributed to mechanical interlocking of features. As deformation proceeds, progressive bending of each pair of interlocking features develops an increasing resistive load which allows the total load to significantly exceed that of the planar roughened case. Work to failure is increased via a combination of increased maximum force, increased displacement enabled by microfeature bending and a more torturous crack path. Low clearances between interlocking features were found to be favourable for mechanical properties owing to reduced bending stiffness of the repeating periodic unit at the interface.

Keywords: adhesion; micro-structured surface; surface texturing; mechanical interlocking; lap joint; strength; toughness.

Corresponding authors: *Daniel M. Mulvihill & Yang Xu, James Watt School of Engineering, University of Glasgow, G12 8QQ, UK. Email: daniel.mulvihill@glasgow.ac.uk and yang.xu@glasgow.ac.uk

1.Introduction

As the demand for increasingly lightweight parts has increased within the automotive and aerospace industry, adhesive bonding has emerged as a prominent method of joining components, owing to its high degree of versatility and ease of assembly [1,2]. Additional advantages of adhesive bonding include effective bonding of dissimilar materials, as well as, removal of the requirement to machine stress raising features such as holes for mechanical fastening. However, the use of adhesive bonding, especially in safety critical applications has been hampered due to a general lack of confidence in the predictability of the strength and toughness of these joints. Varying failure modes can stem from improper surface pre-treatments, varying levels of adhesive coverage, varying bond-line thickness as well as non-uniform peak stresses leading to catastrophic failure. A stress analysis of the single lap joint (SLJ) for flat adherends highlights the issue of stress distribution with high peak stresses and joints failing in a brittle and unpredictable manner under impact loading [3,4]. These issues are exacerbated for adherends composed of polymers due to the lower surface energies resulting in comparably poorer adhesion. Plasma based pre-processing such as corona treatments have been used to increase polymer bond strength for poly-propylene, polycarbonate and poly-ether ether ketone (PEEK), although bond strength is still limited compared to metals [5,6,7].

The goal with adhesive joints is to increase strength, toughness and repeatability. A common practical approach to improving adhesion is to roughen the adherend surfaces. Many researchers have also tested joints having structured adherend surfaces particularly with metals and ceramics. A method that has seen significant attention is laser ablation. Mechanical testing of laser ablated SLJs has shown a marked improvement in joint strength relative to SLJs comprising conventional planar rough surfaces [8,9,10] . The strength and toughness in copper-to-epoxy joints tested in the T-peel test coupon were substantially increased by employing laser ablation in Hernandez *et al*. [11]. The improvement was attributed to chemical modification and mechanical interlocking of the structured surface with the adhesive promoting a cohesive failure in the adhesive layer. Work utilising laser based structuring of

stainless steel in tandem with injection moulding of a plastic to transmit the load was conducted by Byskov-Nielsen *et al*. [12] highlighting the potential to substantially increase mechanical strength via a micro-structured interface

Work relating to actual mechanical interlocking of the adherend features has generally been restricted to the millimetre scale. In the work by Cordisco *et al*. [13], interlocking features were explored with sinusoidal patterns in aluminium double cantilever beam (DCB) joints. Maximum peak load was found to increase with aspect ratio (amplitude/wavelength) and crack propagation was delayed (compared to flat surfaces) under Mode I loading owing to the more torturous crack path. Interlocking square wave features for DCB and butt joint setups have shown strength and toughness improvements due to their introduction of a mixed-mode response which incorporates the stronger shear mode into both joint types [14,15]. Teeth-like profiles in steel were shown to dramatically modify the failure mechanism of the SLJ following an initial fracture with a strength increase of 12% relative to planar samples in [16]. In [17], finite element work by Corbett *et al*. predicted up to 86.5% improvement in work to failure for a SLJ setup composed of a male and female adherend interlocking in shear. Follow-on experimental work looking at optimising the geometry of a single (mm sized) interlocking feature recorded work to failure improvements of up to 542% [18]. In [19], Carbon fibre reinforced plastic (CFRP) prepregs were laminated onto a micro-fabricated steel surface and cured. Results illustrated that the interlocking features led to a more gradual failure which allowed for substantially more joint displacement (and therefore, energy dissipation) before fracture. Hikosaka *et al*. [20], has demonstrated through crack opening tests, that the imprinting of periodic channels results in an increase in Mode I fracture toughness with increasing aspect ratio. This was ascribed to an increase in overall microscopic crack length, an increase in Mode II loading per unit area and transitioning from an interfacial failure to cohesive failure. Research involving polymers is limited: roll-imprinting of polypropylene, with undercut angles ranging from 0° to 35° has been shown to increase strength in butt joints relative to planar samples with mechanical interlocking of the adhesive accounting for the improvement [21].

Looking at the relevant mechanical interlocking and micro-structuring literature in the context of adhesive bonding, it is apparent that there has not been a study in which these have been combined.

Our hypothesis is that truly interlocking micron sized features have the potential to increase both strength and toughness. Micron sized features mean more features per unit length are possible. Therefore, more distributed direct transmission of load into the bulk material (via mechanical interlocking rather than solely through adhesive shear or peel) and a longer bond line for crack propagation are possible. It is also possible that joints that depend more on mechanical interlocking (as opposed to adhesive properties) may have greater repeatability. Thus, we propose to generate true mechanical interlocking of adherends using micron sized features. To enable this approach, a microfabrication protocol combined with injection moulding has been used to produce polycarbonate single lap joint adherends with highly repeatable micro-structuring. Interlocking SLJs are then tested to assess benefits for strength and toughness.

2. Fabrication

This section details the fabrication steps used to produce the micro-structured adherend surfaces.

2.1 Silicon microfabrication

 Standard microfabrication techniques were employed to first create the repeatable square-wave geometries in a silicon master. Photolithography (Fig. 1a and 1b) was used to prepare a pattern of exposed areas for etching. To define the microstructure in the silicon master, deep reactive ion etching (DRIE) was used to etch silicon in a highly directional process (Fig. 1c) resulting in the production of

grating structures with highly vertical sidewalls as represented in Fig 1d. Feature depth can be modified by adjusting etching time.
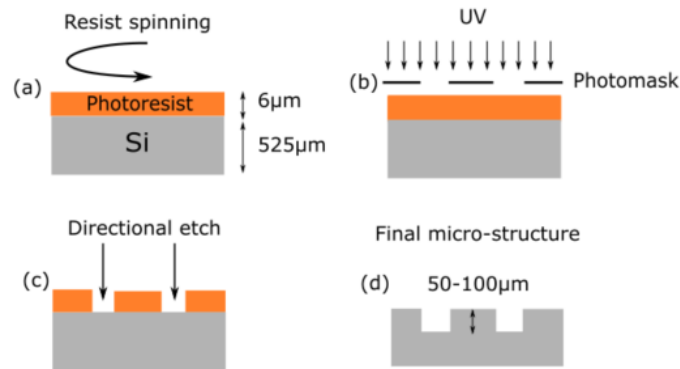

Figure 1: Silicon microfabrication overview: (a) spinning of photoresist; (b) selective exposure of the resist to UV light during photolithography process; (c) anisotropic etching of the exposed silicon and (d) the desired final micro-structure. Detailed information on dimensions is given within Section 3.1.

2.2 Micro-imprinting process

The second step in the process involves transferring the pattern from the silicon master into a material with suitable thermal properties as well as durability to be used as a mould inlay. This was done using a modified nanofabrication protocol: Fig. 2 conveys the key stages. The silicon master is covered in an anti-stick layer (to enable separation of the wafer and stamp material) with a substance known as the working stamp material spun on top of the wafer (Fig.2a). The wafer is then placed in a tool where the working stamp layer is imprinted onto a new transparent layer of Polyethylene terephthalate (PET) and subsequently UV-cured (Fig.2b), resulting in the inverse pattern from the silicon wafer being formed on the new PET sheet.
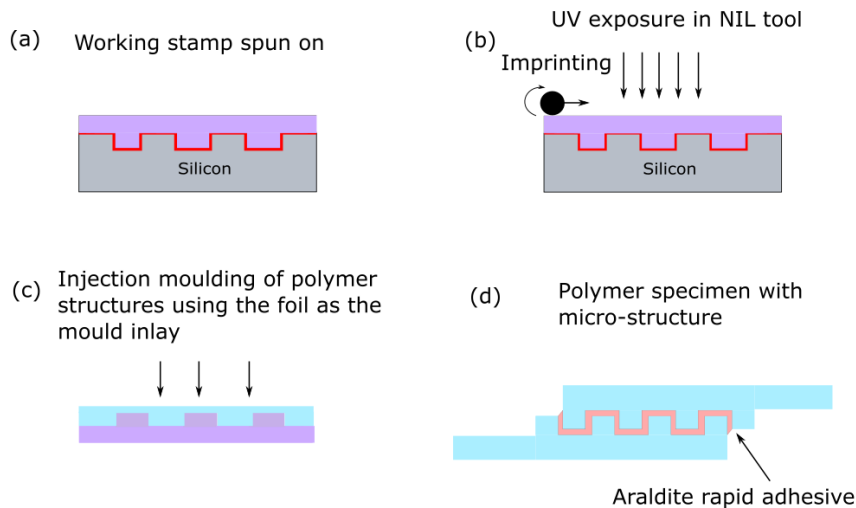
Figure 2: Mould inlay fabrication overview: (a) spinning of a working stamp material (purple) on top of the structured silicon master - an anti-stick layer (red) is spun initially to enable separation from the silicon substrate; (b) imprinting of the micro-features from the silicon to the working stamp material, followed by UV curing to solidify the mould insert; (c) injection moulding using the mould insert for the production of micro-structured polycarbonate specimens (blue) and (d) the final interlocking bonded lap joint with Araldite rapid adhesive (pink).

2.3 Injection moulding

The final step in the fabrication process is the use of injection moulding to obtain the micro-structured pattern (Fig. 2c) in a mechanically suitable material. Polycarbonate was chosen as the sample material owing to its excellent toughness properties. The key parameters that characterise the moulding process are mould temperature, polymer injection temperature, injection velocity, pressure and the cooling time. Optimising the moulding conditions ensures sufficient filling of the micro-cavities to replicate the geometric fidelity from silicon master to polycarbonate. Injection moulding was performed using an Engel Victory 28 fully hydraulic injection moulding machine with a melt temperature of 270°C and a tool temperature of 70°C used. The PET foil supporting the pattern was laser cut to dimensions of 75mm x 25mm and placed inside a tool hardened steel frame. The polycarbonate was dried for a minimum of 2 hours at 110°C in a vacuum oven prior to moulding.

Fig. 3 shows a scanning electron micrograph of the moulded polycarbonate. Due to the mould tooling, the part thickness was limited to 1 mm. Following injection moulding, the samples were cut using a guillotine to dimensions of 7.5 mm x 40 mm (for the structured samples, only a 7.5 mm stretch near one end of the 40 mm length is structured).
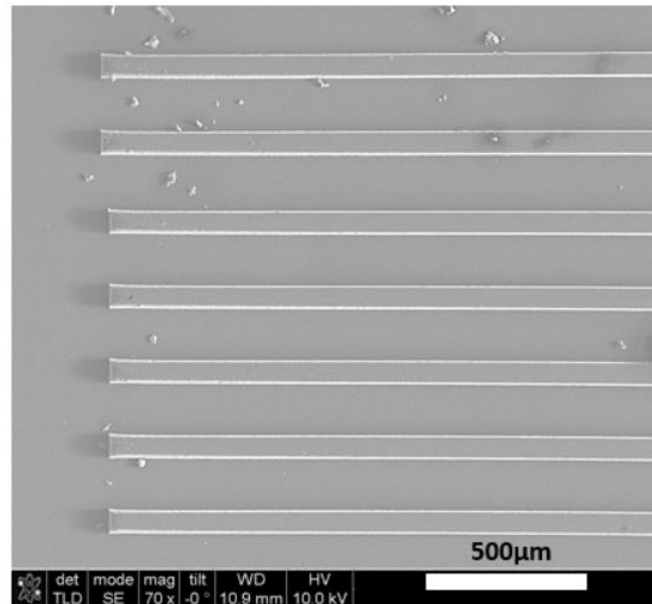

Figure 3: Scanning electron micrographs of moulded polycarbonate grating structure - top down view at x70 magnification.

3. Testing

3.1 Preparation of joints

Samples were then overlapped by 7.5 mm to produce a bonded area of 7.5 x 7.5mm. Fig. 4 shows a schematic of a joint. For the structured interfaces, the full bond area is structured with the square-wave micro features. Bonding was carried out using a 2-component epoxy, Araldite Rapid with a curing time of 4 hours at room temperature, in accordance with the manufacturers guidelines [22]. For the structured joints, the work required a significant level of user expertise in ensuring that the two structured parts were truly interlocking. This was also checked later using an optical microscope. Material properties derived from tensile testing of the adhesive are given in Table 1.
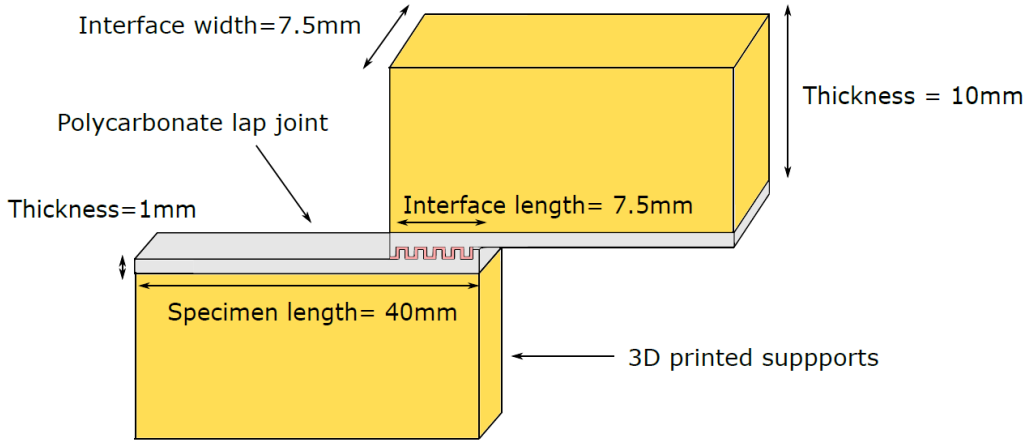
Figure 4: Schematic diagram and dimensions for a structured interlocking joint. Samples (grey) were cut to a length of 40 mm and bonded to thicker custom supports (orange) designed to prevent bulk failure of the polycarbonate. The dimensions of the structured bonded interface are 7.5 mm x 7.5 mm.

Table 1: Material properties for the Araldite rapid adhesive obtained via tensile testing of standard dog-bone samples.

E (GPa)	UTS (MPa)	ε (failure) (%)
0.49 ± 0.06	6.3 ± 0.65	0.29 ± 0.04

Fig. 5 shows the key feature/channel dimensions: feature depth D, feature width λ_f, channel width λ_c and total horizontal clearance c.
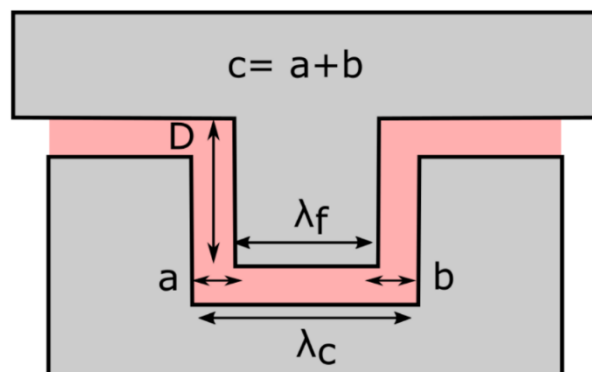

Figure 5: Schematic showing single interlocking feature with polycarbonate (grey) bonded by adhesive (pink): D denotes feature depth, λ_f denotes feature width, λ_c denotes channel width, a and b denote clearance at each side of the feature and C denotes total clearance.

Three different feature clearances and two different feature depths were chosen to allow investigation of the effect of clearance and feature depth. The categories are summarised in Table 2

with feature width, λ_f remaining constant at 100µm and three different channel widths λ_c of 150, 200 and 300 µm used to give clearances of 50, 100 and 200 µm. To assess the performance of the structured interfaces against a benchmark, joints with unstructured adherends were also tested. Flat unabraded polycarbonate (denoted as 'planar untreated') and flat P80 grit sandpaper roughened (denoted as ''planar roughened') polycarbonate joints were the two unstructured instances chosen. The roughened surface is more representative of the properties achievable with nominally planar unstructured joints.

For the structured parts, quantification of the feature geometry was performed using a Bruker contour GT optical profiler, to determine the deviation in size from the initial silicon master to the moulded part. For both the 50µm and 100µm depths, the feature heights were found to be slightly reduced from the initial silicon master. This result was anticipated as there is inevitably some polymer shrinkage during the holding phase of the mould cycle. Likewise, feature widths were found to be reduced across all categories due to the polymer shrinkage, preventing the channels within the mould inlay from filling completely; this finding was more pronounced with the 100µm deep structures. Nonetheless, the samples were perfectly adequate for interlocking. The evolution of the key feature dimensions from nominal design values to silicon master to final polycarbonate specimens are given in Table 2. Fig.6 shows the typical variation between moulded part and initial design surface for the case with a feature depth of 100µm and a clearance of 50µm. Due to the partial shrinkage associated with injection moulding during the filling phase, the feature corners had a more rounded geometry compared to the step-like gratings initially obtained from etching and the nano-imprint process. Although not intentional, this will be advantageous in reducing stress concentrations around feature corners.

Table 2: Test categories table: Designed feature dimensions and mean measured values for the silicon master and polycarbonate (PC) samples alongside standard deviations (in brackets). Parameters are: Clearance C, feature depth D, feature width λ_f and channel width λc, corresponding to the descriptions in Fig. 5.

Clearance (C)	Feature depth (D)			Feature width (λ_f)			Channel width (λ_c)		
Design (µm)	Design (µm)	Silicon (µm)	PC (µm)	Design (µm)	Silicon (µm)	PC (µm)	Design (µm)	Silicon (µm)	PC (µm)
100	50	51.7 (0.03)	48.0 (0.09)	100	93.9 (0.94)	82.8 (5.35)	200	202 (3.18)	227 (2.83)
200	50	51.7 (0.03)	48.0 (0.17)	100	94.4 (0.75)	78.6 (2.57)	300	304 (1.44)	325 (3.91)
50	100	101 (0.19)	98.9 (0.05)	100	94.8 (2.45)	77.3 (5.33)	150	153 (1.79)	170 (3.85)
100	100	103 (0.13)	94.3 (0.66)	100	93.5 (2.21)	74.2 (2.29)	200	206 (2.16)	226 (2.26)
200	100	102 (0.49)	94.4 (0.90)	100	93.0 (4.70)	69.4 (1.01)	300	307 (2.25)	331 (1.10)

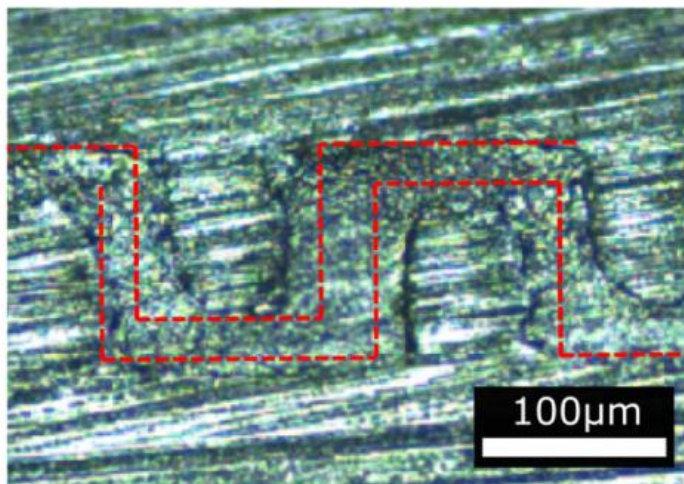

Figure 6: Comparison of as-moulded surface with initial design surface (in red). For this case, the design dimensions were: feature width λ_f,=100µm, channel width λ_c =150µm and depth D=100µm while the average measured dimensions of the as-moulded surface were: λ_f,=77.3µm, λ_c =170µm and D=98.9 µm.

Optical profile measurements were taken to quantify the surfaces of the unstructured polycarbonate samples: untreated and P80 roughened. The untreated surfaces were sputtered with gold palladium (transparent surfaces may lead to image artefacts during optical profilometry) and imaged using a contour GT profiler owing to the nanometre scale roughness, while the roughened surfaces were imaged using an Alicona G4 profiler (a system more adept for imaging rougher surfaces). Three samples were analysed for both the untreated and roughened groups, with three scans taken in the longitudinal and perpendicular directions. Roughness parameters average roughness (R_a), root mean square roughness (R_q) and maximum height (R_z) were determined: these are given in Table 3 . The untreated samples have a very low roughness in the nm range while the P80 roughened samples have roughness in the 2-3 micrometre range. The roughened samples were tested to provide a more representative benchmark (i.e. that typical of standard abrading pre-treatment).

Table 3: Surface roughness data for the untreated planar samples and planar P80 roughened samples alongside standard devaitions. Measurements were taken in the perpendicular and longitudinal directions.

Parameter	Untreated Planar		Planar P80 roughened	
	Longitudinal	Perpendicular	Longitudinal	Perpendicular
Ra (nm)	32 ± 21	35 ± 27	2380 ± 647	2777 ± 685
Rq (nm)	41 ± 20	48 ± 32	3060 ± 811	3983 ± 402
Rz (nm)	403 ± 112	320 ± 130	12963 ± 2945	16023 ± 4920

3.2 Testing

To enable single lap-joint testing of the moulded parts, custom test fixtures were required. An image of the test setup is given in Fig. 7. The main testing limitation was the 1 mm thickness of the moulded parts. To prevent bulk failure of the polycarbonate, specimens were bonded to thicker supporting fixtures. This setup provides a means to resist the bending moment that would otherwise lead to premature bulk failure of the joint. These parts were 3D printed using a Form-2 3D printer using clear resin and bonded to the back of the specimens via adhesive. The specimen-to-fixture bond extended

from the outer interface edge to the inner fixture edge close to the loading pins. Since this bonding length of 40 mm for the support fixture was substantially longer than the interface length of 7.5 mm, this ensured failure occurred exclusively within the lap joint, instead of de-bonding of the specimen backing from the holding fixture. The custom test setup was integrated into a Deben micro-tensile tester using custom made stainless steel connecting fixtures with loading pins.
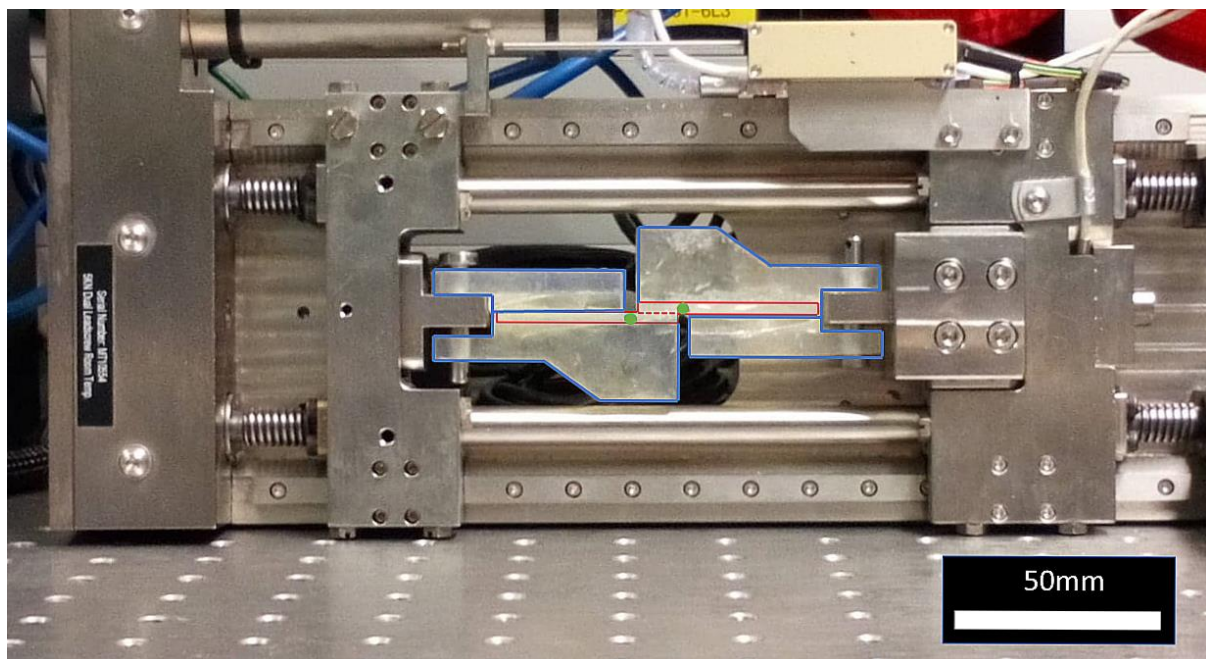

Figure 7: Deben micro-tester with integrated 3D printed test fixtures to prevent bulk failure of the polycarbonate bonded joint during testing. The blue outline denotes the 3D printed support structures, with the red lines denoting the polycarbonate lap joint. The green circles located at the edges of the interface denote the locations used for tracking relative displacement.

The extension during the test was 0.5 mm per minute with a sampling rate of 2 Hz to record the force. A local measurement of the strain was achieved through tracking marker points just outside either end of the bond-line. Images were acquired using a pixel-link camera facing the side of the interface at the same sampling rate as the micro-tester. Strain data was determined using Imetrum digital image correlation software to determine the relative displacement between the two marker points. Load was taken directly from the 5 kN Deben microtester load cell. Tests were repeated five times with new specimens for each test category.

4.Results and discussion

4.1 Mechanical test results

The nominal shear stress versus strain graphs for the planar untreated and planar roughened samples are given in Fig. 8a. The nominal shear stress values were obtained as an average stress by dividing the tensile force by the nominal area of the interface (7.5 x 7.5 mm). The planar samples failed adhesively with the roughened samples typically exhibiting a mixed adhesive/cohesive failure. As anticipated, the shear strength values obtained for the roughened samples were generally greater than the untreated samples. The mean maximum shear stress for the untreated samples was 3.96 +/- 0.73MPa compared to 5.75 +/- 0.77MPa for the roughened specimens. Strain to failure (and hence work to failure) is also clearly higher for the roughened specimens. Improved mechanical properties for the roughened specimens are to be expected since the increased surface roughness will increase bonding surface area (by an average of 1.3 times here), permit a degree of interlocking with the adhesive and increase the 'effective compliance' of the interface.

The stress-strain graphs for the structured interfaces (at feature depths of 50 and 100 μm) are given in Fig. 8b and Fig. 8c, respectively, for each of the three clearances tested. The mean joint strength values for all joint types are summarised in Fig. 9 with error bars indicating variability. All structured cases resulted in significantly higher mean strength as compared to the planar untreated and planar roughened interfaces. As Fig. 9 shows, for 50 μm feature depth, mean joint strengths were nearly constant over the three clearance instances exhibiting increases in the range of 57.2 to 60.8% over the planar roughened joint. For the 100 μm depth, strength increased with reducing clearance ranging from an increase of 23.3% over planar roughened for the 200 μm clearance to 95.8% for the 50 μm clearance. There does appear to be some variation in the failure modes (see Fig. 8) with some samples exhibiting a gradual more ductile load response and others failing in a more brittle fashion at lower strain values – the reason for this is not entirely clear, but is likely to be due to variations in exactly how the joint was assembled and bonded.
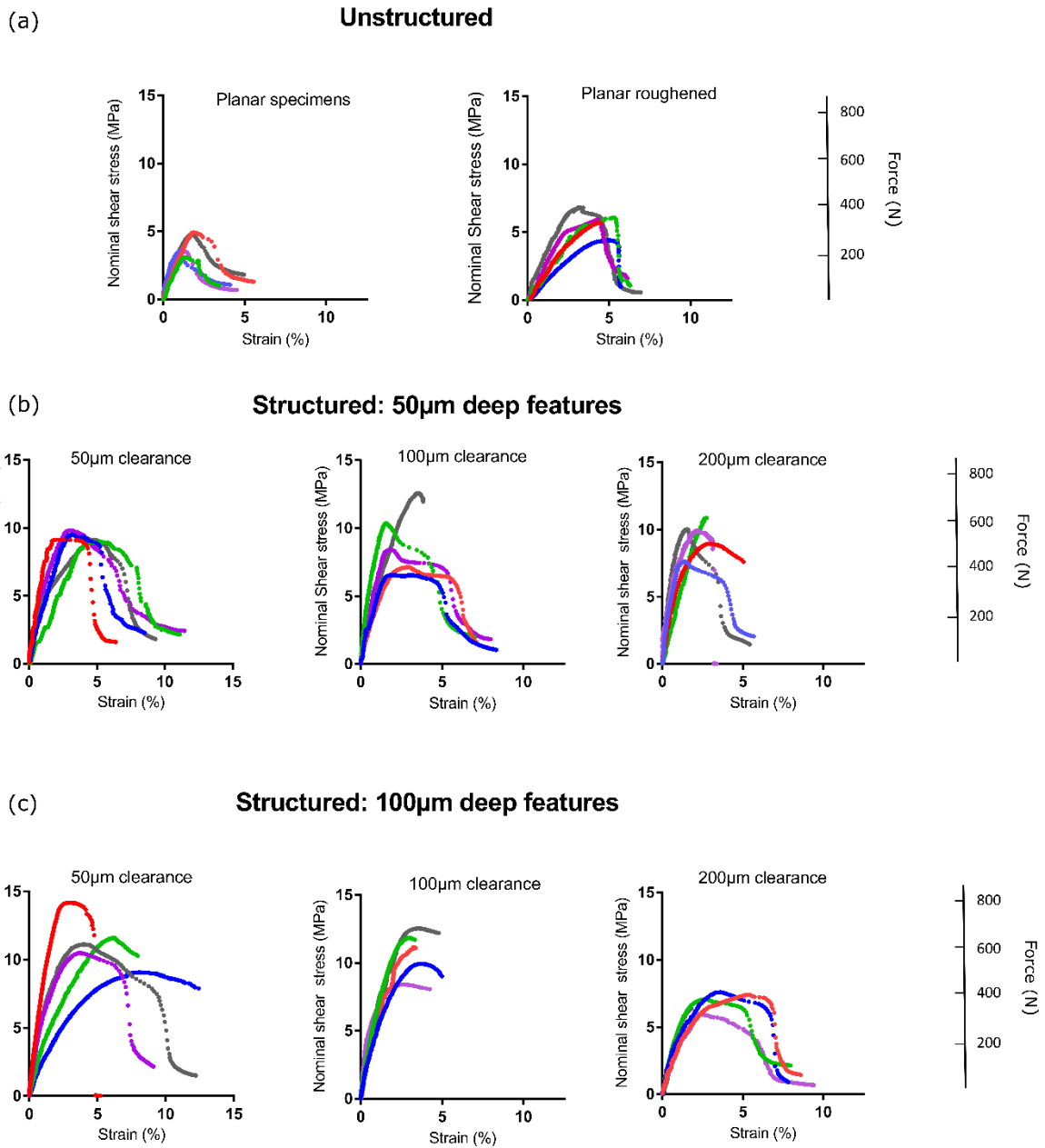
Figure 8: Nominal shear stress versus strain data for all tests: (a) unstructured tests (planar untreated and planar roughened); (b) structured with 50 μm deep features having clearances C = 50, 100 and 200 μm and (c) structured with 100 μm deep features also having clearances C = 50, 100 and 200. Different line colours on each graph represent repeat tests.
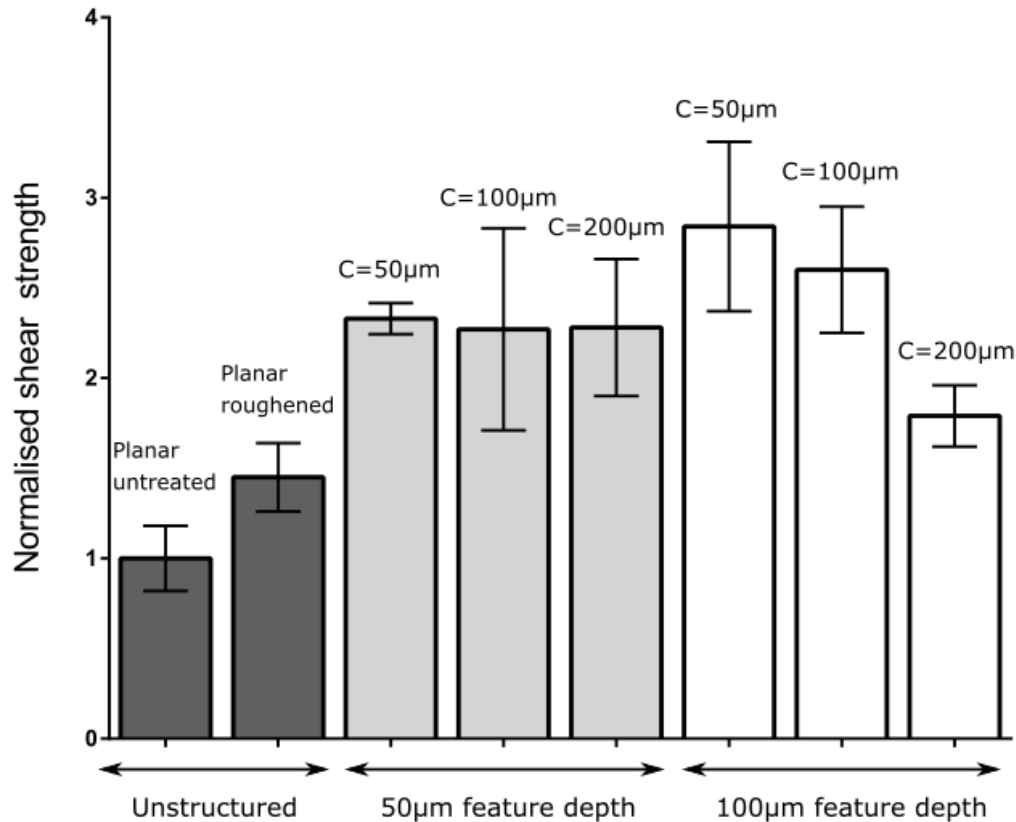
Figure 9: Normalised nominal shear strength relative to the planar untreated sample for each test category (+/-SD). Dark grey bars: planar untreated and planar roughened. Light grey bars: structured interfaces with 50μm deep features. White bars: structured interfaces with 100μm deep features. For the structured tests, the clearance *C* is labelled above each bar.

The work to failure for each test group was calculated as the area under the force-extension graphs. The resulting mean values and variability are shown in Fig 10. In general, the structured joints absorbed more energy than the planar roughened case. The tightest clearance instance (i.e. *C* = 50 μm) gave notably higher work to failure for both the 50 and 100 μm depths. These gave increases in work to failure of 161 and 162 %, respectively, over the planar roughened case. This is because the tighter clearance case, in general, permitted both greater maximum load and greater displacement to failure (Fig. 8). Based on all of the cases studied, Figs. 9 and 10 indicate the *C* = 50 μm, *D* = 100 μm case is optimum as this exhibits the best combination of both strength and work to failure (95.8% increase in strength and 162% increase in work to failure over the planar roughened case).
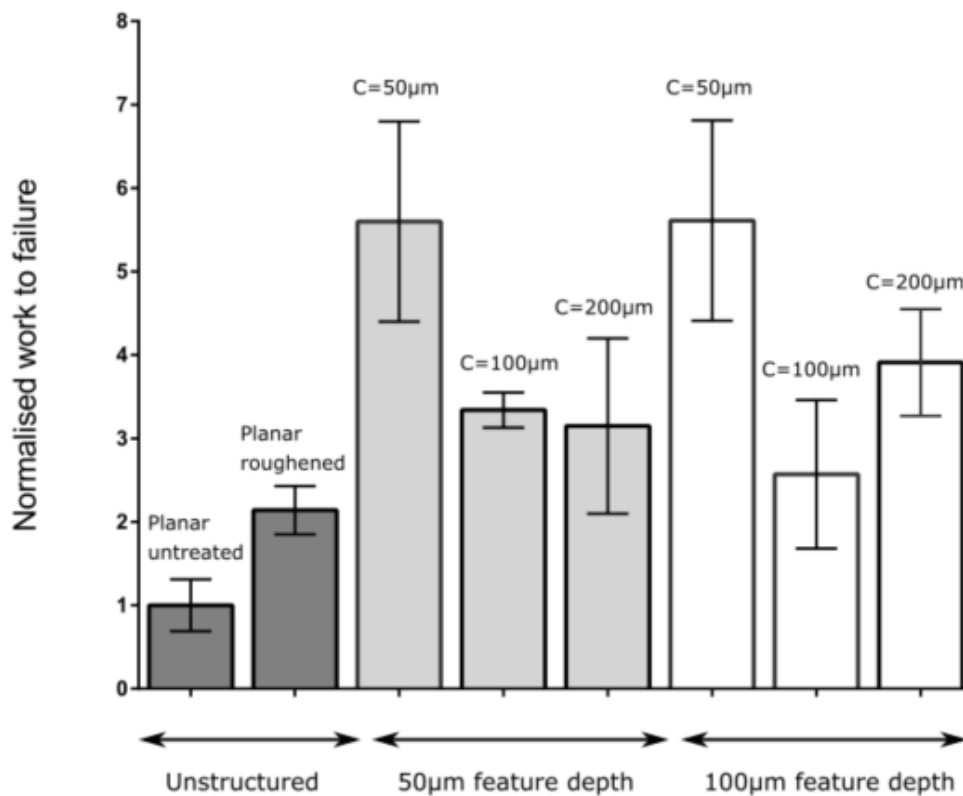
Figure 10: Normalised work to failure relative to the planar untreated sample for each test category (+/- SD). Dark grey bars: planar untreated and planar roughened. Light grey bars: structured interfaces with 50μm deep features. White bars: structured interfaces with 100μm deep features. For the structured tests, the clearance C is labelled above each bar.

Doubling the feature depth from 50 to 100 μm does not seem to have had a definitive effect: the mean strengths for the 50 and 100 μm clearance increased by 21.7 and 14.5 %, but reduced by 21.5 % for the 200 μm case, while the mean work to failure (Fig. 10) was similar for the 50 μm clearance, reduced by 23.2% for the 100 μm clearance and increased by 24% for the 200 μm clearance. A definitive trend with a parameter like feature depth may be difficult to observe owing to variability in the results. There are several sources of variability including the location the features take up within the channels during bonding, the adhesive coverage of the interface surface area, and the true interpenetration depth of one set of features with another.

4.2 *In-situ* bond-line imaging

In-situ tests allowing concurrent microscope imaging of the bond-line during testing were carried out to visually investigate the mechanisms governing the mechanical response of the structured joints. Two tests were conducted: one on the interface with 100 μm deep features with 50 μm clearance and one on the interface with 100 μm deep features with 200 μm clearance (i.e. the minimum and maximum clearance cases for the 100 μm deep features). One side of the joint was polished to enable imaging of the bond-line. Polishing was conducted using a Struers LaboSystem mechanical polisher with silicon carbide papers starting with P280 grade and further refining with P800 and P1200 grade paper. All testing conditions remained the same as the previous testing to ensure the results were comparable. Imaging of the polished side of the joint was performed during testing using a Alicona G4 profiler with a 10X objective lens. As testing progressed and the features became increasingly distorted, the magnification was increased to x20 to adequately image the interface.

The *in-situ* test results are given in Fig. 11 for the 50 μm clearance and Fig. 12 for the 200 μm clearance case. Figs. 11(a-d) and Figs. 12 (a-d) show images of part of the interface at key stages of joint deformation while Fig. 11e and Fig. 12e give the associated stress-extension curves with markers denoting the location on the curve corresponding to the images in (a-d). The imaging was conducted near the edges of the bond-line, corresponding to the purple square denoted on the accompanying inset schematic in Fig. 11 and Fig.12. Note that the bending direction of the features in Figs. 11 and 12 are opposite from one another. This was due to the two different positions possible when loading the lap joint; this is clarified in the inset schematic.
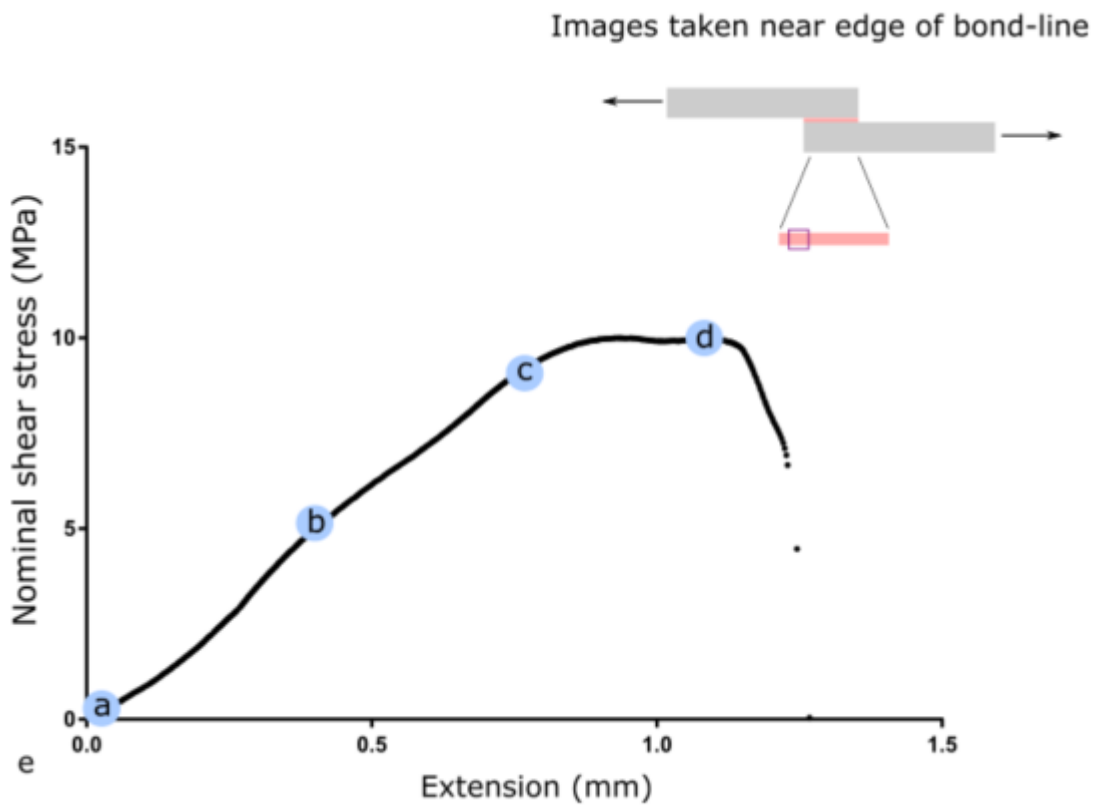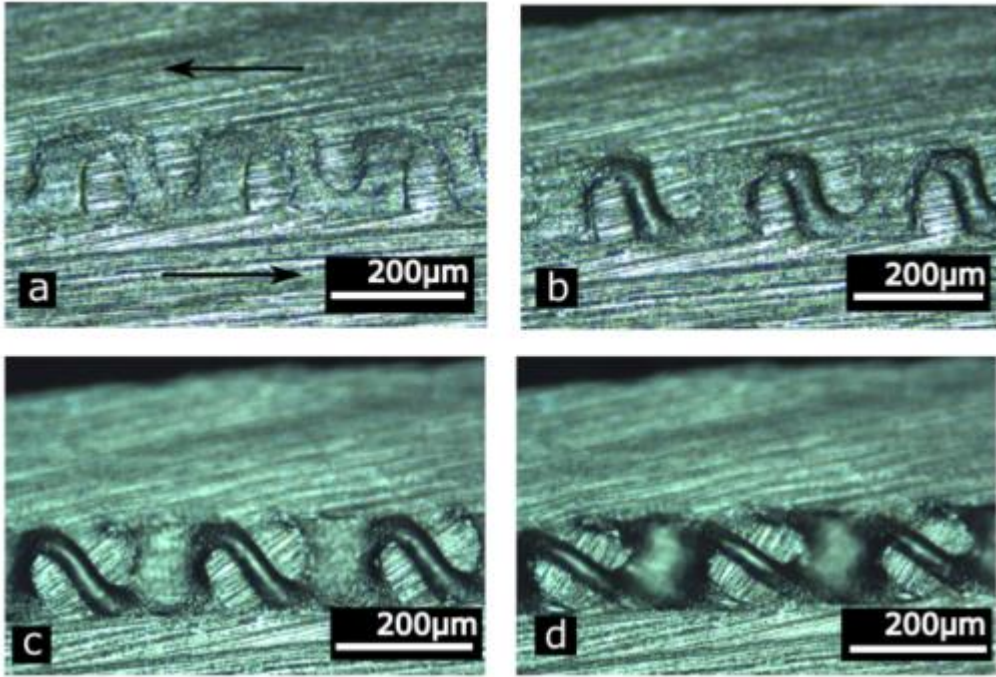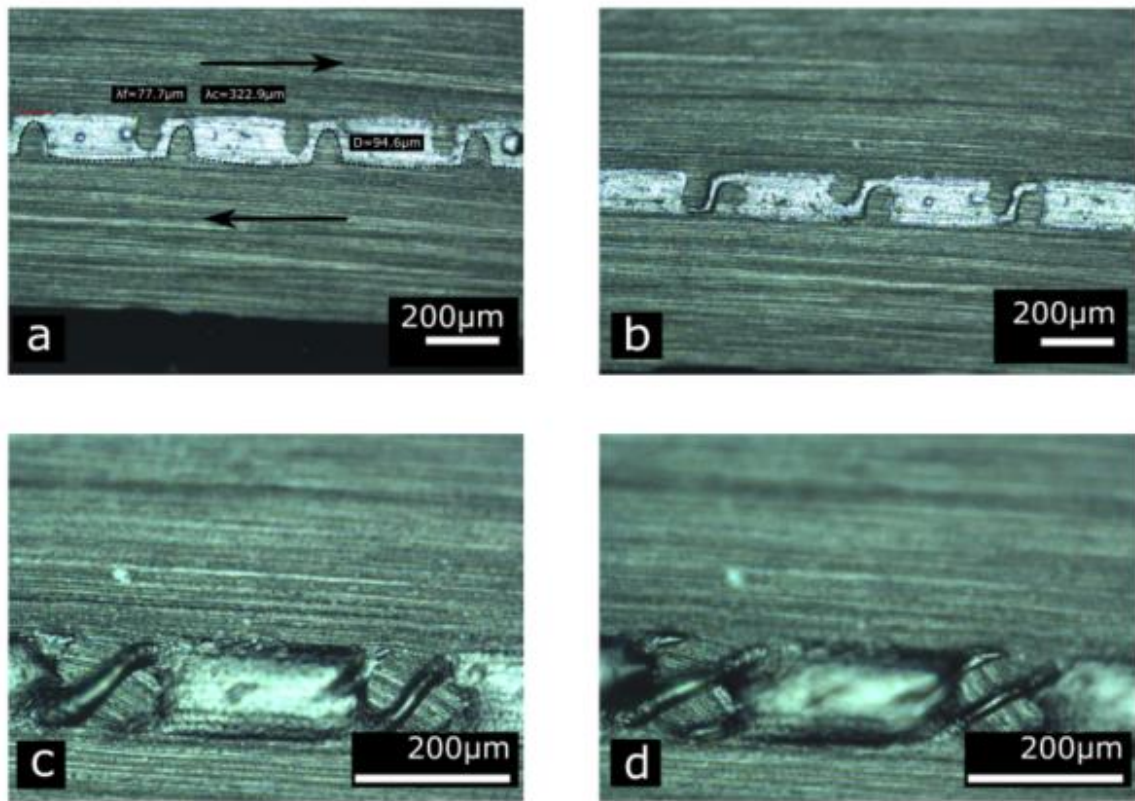
Figure 11: Narrow clearance in-situ results, (a) to (d): Side-on microscope images of a portion of the interface at key stages of lap-joint deformation for the structured surface with features having depth D = 100 μm and clearance C = 50 μm. (e) Nominal shear stress versus extension showing the stages on the loading path corresponding to the images in (a) to (d).
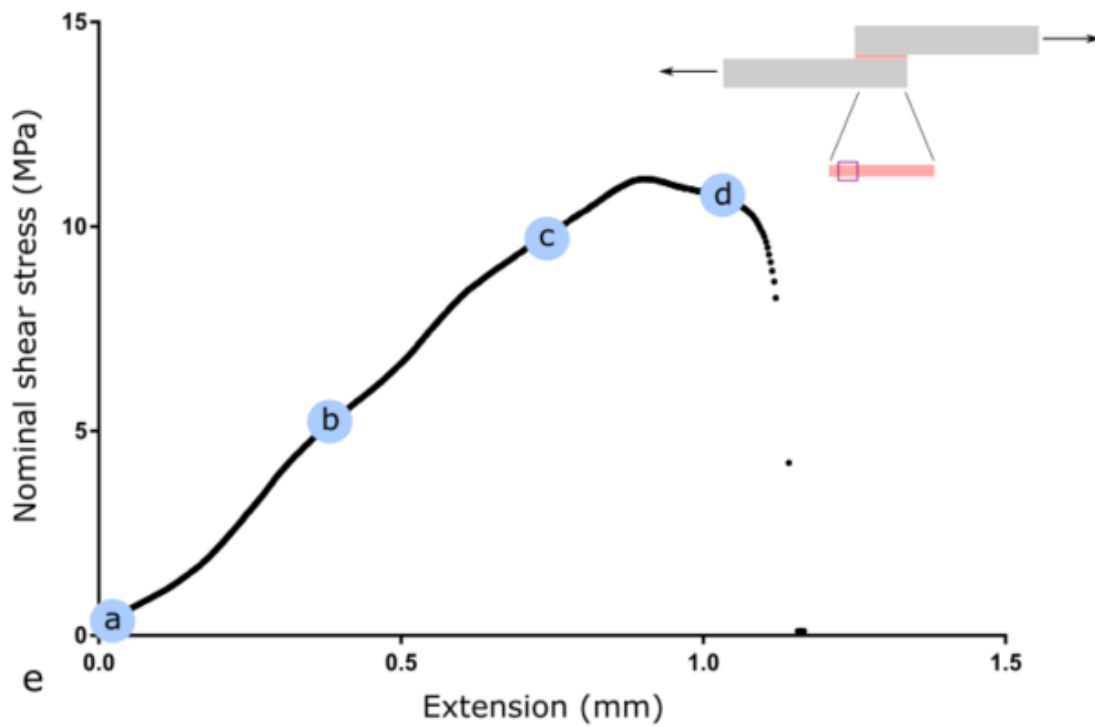
Figure 12: Wide clearance in-situ results, (a) to (d): Side-on microscope images of a portion of the interface at key stages of lap-joint deformation for the structured surface with features having depth D = 100 µm and clearance C = 200 µm. (e) Nominal shear stress versus extension showing the stages on the loading path corresponding to the images in (a) to (d).

Image (a) in Figs. 11 and 12 shows the unloaded interface. Image (b) shows the interface at a load sufficient to fail the planar roughened samples. From image (b) onwards, there appears to be darker regions around the features – this is caused by movement of the adhesive such that it appears out of focus. After Image (b), the joint is achieving strength and work to failure above that achieved by the planar roughened joint: the reason for this is the mechanical interlocking. Images (c) and (d) illustrate the mechanism: the resistance afforded by the interlocking features is evident in the progressive bending of the features up to the very severe bending apparent in Image (d) which is taken just before failure of the joint. Referring to the simple example of deflection of a cantilevered beam, we note that the force required increases as deflection proceeds. The features in the structured interfaces are analogous to an array of deflecting cantilevered beams each sharing a portion of the increasing resistive load. Thus, the strength of the joint is increased. The mechanism also increases work to failure due to the higher forces achieved. Additionally, the severe feature bending permits further joint displacement prior to failure. At a certain point between (c) and (d), the joint yields and the feature bending is so severe that it can no longer sustain increases in load. There is some further extension before catastrophic failure of the joint and the features then slide over each other. In the latter stages of joint deformation (after the max load is reached), localised ductile ruptures of the adhesive were apparent between the features (now deflected at large angles). Local failures then coalesce to produce complete failure of the joint. The torturous nature of the bondline means that more energy can be dissipated before the joint is fully separated. Fig. 13 shows a side-on microscope image of one half of the post-test interface for the 50 µm clearance case (i.e. corresponding to the test results given in Fig 11). Despite the severe feature bending evident during the test, the features remain intact after the test and no adherend failure is apparent. The features in Fig. 13 have recovered somewhat from the degree of bending evident in Figs 11 (d) and 12 (d), but, some plastic deformation is apparent. The residual presence of adhesive in Fig. 13 suggests a cohesive failure of the adhesive.
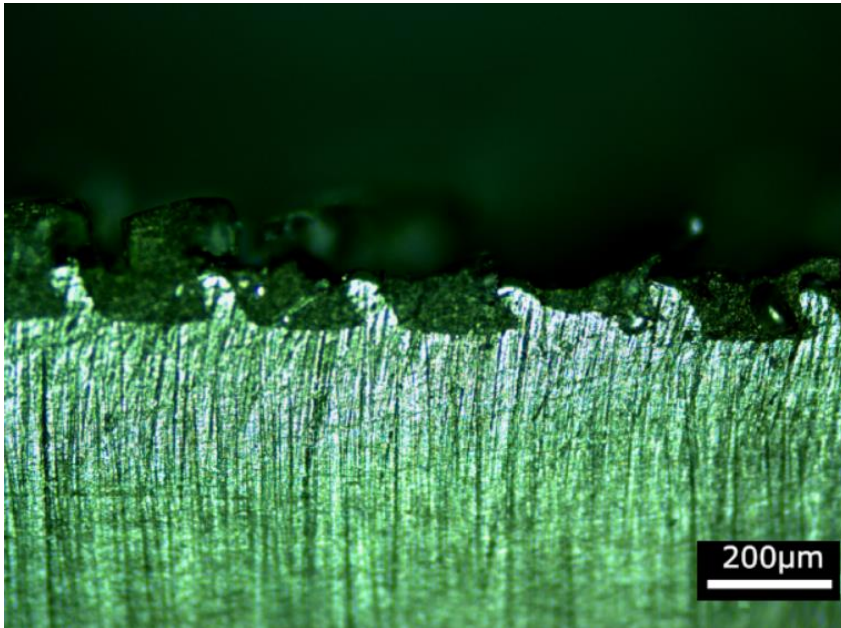
Figure 13: Optical side-on microscope image of one half of a failed structured interface. The image was taken at the edge of the joint. The sample had 100 µm deep features with a 50 µm clearance and corresponds to the test in Fig. 11.

We can also re-examine the effect of clearance in light of the bending mechanism discussed above. Recall that tighter clearance resulted in greater work to failure (Fig. 10). If we imagine a periodic repeating bending unit at the interface consisting of feature and adhesive (as depicted in Fig. A1 in the Appendix), then the bending stiffness of that unit will be decreased as the adhesive filled clearance between the features reduces – this is explained by recourse to sandwich beam bending theory (see Appendix). Reduced bending stiffness means more displacement is permitted, and thus, more work can be done. For the *in-situ* test on the largest clearance case (C = 200 µm) in Fig. 12a, the features happened to be positioned close to each other resulting in rather similar stress-extension graphs for the C = 50 µm and C = 200 µm cases (i.e. Figs 11e and 12e). However, other attempts at assembling the joint will likely have seen the higher clearance features bonded at a greater separation distance (such as for the tests leading to Figs. 8 to 10). Indeed, the variation in work to failure with clearance for the D = 50 µm case in Fig 10 must be due to greater joint displacement as the loads to failure for this case (Fig. 9) are almost constant with clearance.

It should be noted that the lap-joint in these tests was constrained by the backing fixtures such that out-of-plane movement (driven by the single lap joint bending moment) was restricted (see Fig. 4 and Fig. 7) and it is likely that a free lap-joint would behave somewhat differently. For example, it is not certain that interlocking features on more typical slender (and unconstrained) lap joints would produce as much of an effect as joint rotation may tend to promote a Mode 1 opening and perhaps less feature bending, but this remains to be investigated further. The fabrication process outlined has applicability for use with typical injection moulding polymers including polystyrene, polypropylene and poly ether ether ketone (PEEK). At present, the process is limited to use with polymers owing to the utilisation of injection moulding to create the final parts. However, micro-structured joints from metal adherends are possible - e.g. nickel electroplating from an etched silicon master. It is anticipated that the feature bending mechanism observed for the polycarbonate adherends would also be present to some degree in an equivalent metallic joint. However, since metallic substrates typically have lower ductility than polycarbonate, it is reasonable to expect less pronounced improvement particularly in work to failure. Another point requiring further investigation is the extent to which the structured interface can redistribute the stress peaks present at the ends of the classical lap joint.

5. Conclusions

The potential of mechanically interlocking micro-structured adherends to increase the strength and toughness of single lap joints is investigated. A fabrication protocol has been established to enable the manufacture of interlocking (square wave) micro-structured joints in thermoplastic polymer (polycarbonate) adherends. The micron-scale structuring is achieved through microfabrication techniques in tandem with injection moulding to produce replicas in polycarbonate. The parts were then bonded as single lap joints in an interlocked configuration and tensile tested using an adapted micro-tensile tester. Planar untreated and planar roughened joints were also tested to provide a benchmark. Compared to the planar roughened joints (Ra = 2-3 μm), results for the micro-structured joints revealed an increase of up to 95.9% for strength and up to 162% for work to failure. The increase in mechanical properties above that of the planar roughened joint is due to the mechanical interlocking. As applied displacement on the joint is increased, each pair of interlocking features contributes to an increasing resistive load via progressive bending of the feature pair. This proceeds to a severe level of bending until the features are no longer able to sustain increases in load. The adhesive then fails cohesively, and the features slide past each other. The mechanism facilitates increases (over the planar roughened case) in macroscopic load and displacement owing to the local feature bending mechanics resulting in corresponding increases in both strength and work to failure. Work to failure in the latter stages of joint deformation is also likely to be enhanced by the tortuous crack path required for cohesive failure in the structured interfaces. The effect of feature clearance was examined by testing three clearance options. The tightest clearance gave the optimum mechanical properties, probably because feature pairs separated by smaller distances have lower bending stiffness (thereby increasing displacement and work to failure). Variation and oscillation in strength and work to failure values as the clearance was varied was attributed to variations in the joint assembly such as feature positioning, adhesive coverage and degree of feature interpenetration. The effect of feature depth was also studied using two feature depth options: 50 and 100 μm, but this had little effect on mechanical properties. The mechanical response of the structured joint (with the

bending mechanism observed) is very different from the planar lap joint case where detrimental stress peaks occur near the ends of the bond-line. Structured interlocking may facilitate a somewhat more even distribution of loading over the joint. In summary, the method has shown significant promise for increasing strength and toughness. Further investigation of the interlocking mechanism will be required to improve understanding and facilitate optimisation using a computational approach.

Acknowledgements

Appendix

The increase in work to failure with reducing clearance can be explained using engineering sandwich beam theory. Selecting one periodic portion on the adhesive interface, we may use a sandwich beam to approximate this composite periodic structure in bending, see Fig. A1. The core and the two face sheets of the sandwich beam are adhesive (thickness $C/2$) and polycarbonate (thickness $\lambda_f/2$), respectively. The flexural stiffness of this sandwich beam is then (from [20]):

$$K = E_p \left(\frac{1}{12} \lambda_f^3 + \frac{1}{8} \lambda_f^2 C + \frac{1}{16} \lambda_f C^2 \right) + \frac{1}{96} C^3 E_{ad} \qquad \text{(A1)}$$

For a fixed feature depth D, the squarewave width λ_f is also constant. Therefore, as clearance C reduces, the flexural stiffness K also reduces. Thus, we can expect greater displacement (and hence work to failure) for joints having tighter clearances. This is borne out in the experimental results of Fig. 9. Note that, in Fig. 8, the failure load is roughly constant with clearance for the D = 50 µm case and hence displacement must be responsible for the variation of work to failure with clearance apparent in Fig. 9. For the D = 100 µm case, failure load also increased with decreasing clearance and hence, in this case, failure load, as well as max displacement, will contribute to the variation with clearance. Note: E_p and E_{ad} are the Young's moduli of polycarbonate and adhesive respectively.
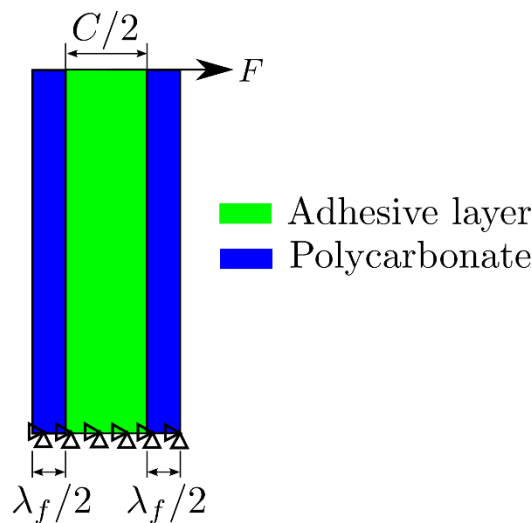

Fig. A1: Sandwich beam theory analysis of periodic feature-adhesive repeating unit. *F* = (total tangential force)/(number of repeating square wave cells).

References

[1]   G. Michalos, S. Makris, N. Papakostas, D. Mourtzis, and G. Chryssolouris, "Automotive assembly technologies review: challenges and outlook for a flexible and adaptive approach," *CIRP J. Manuf. Sci. Technol.*, vol. 2, no. 2, pp. 81–91, Jan. 2010.

[2]   A. Higgins, "Adhesive bonding of aircraft structures," *Int. J. Adhes. Adhes.*, vol. 20, no. 5, pp. 367–376, 2000.

[3]   O. Volkersen, "Die Niektraftverteiling in Zugbeanspruchten mit Konstanten Laschenquerschritten.," *Luftfahrtforschung*, vol. 15, pp. 41–47, 1938.

[4]   E. Goland, M. and Reissner, ""The stresses in cemented joints," *J. Appl. Mech.*, vol. 11, pp. A17–A27., 1944.

[5]   S. Kitova, M. Minchev, G. Danev, and B. Academy, "Rf plasma treatment of polycarbonate substrates," *J. Optoelectron. Adv. Mater.*, vol. 7, no. 5, pp. 2607–2612.

[6]   N. V Bhat and D. J. Upadhyay, "Plasma-Induced Surface Modification and Adhesion Enhancement of Polypropylene Surface," *J. Appl. Polym. Sci.*, vol. 86, no. 4, pp. 925–936.

[7]   J. Comyn, L. Mascia, G. Xiao, I. E, and B. M. Parker, "Corona-discharge treatment of polyetheretherketone (PEEK) for adhesive bonding," *Int. J. Adhes. Adhes.*, vol. 16, no. 4, pp. 301–304, 1996.

[8]   X. M. Zhang, T. M. Yue, and H. C. Man, "Enhancement of ceramic-to-metal adhesive bonding by excimer laser surface treatment," *Mater. Lett.*, vol. 30, no. 5–6, pp. 327–332, Apr. 1997.

[9]   E. G. Baburaj, D. Starikov, J. Evans, G. A. Shafeev, and A. Bensaoula, "Enhancement of adhesive joint strength by laser surface modification," *Int. J. Adhes. Adhes.*, vol. 27, no. 4, pp. 268–276, 2007.

[10]   M. Alfano *et al.*, "Surface Patterning of Metal Substrates Through Low Power Laser Ablation

for Enhanced Adhesive Bonding," *J. Adhes.*, vol. 90, no. 5–6, pp. 384–400, 2014.

[11]   E. Hernandez, M. Alfano, G. Lubineau, and U. Buttner, "Improving adhesion of copper/epoxy joints by pulsed laser ablation," *Int. J. Adhes. Adhes.*, vol. 64, pp. 23–32, 2016.

[12]   J. Byskov-Nielsen, J. V. Boll, A. H. Holm, R. Højsholt, and P. Balling, "Ultra-high-strength micro-mechanical interlocking by injection molding into laser-structured surfaces," *Int. J. Adhes. Adhes.*, vol. 30, no. 6, pp. 485–488, 2010.

[13]   F. A. Cordisco, P. D. Zavattieri, L. G. Hector, and B. E. Carlson, "Mode i fracture along adhesively bonded sinusoidal interfaces," *Int. J. Solids Struct.*, vol. 83, pp. 45–64, 2016.

[14]   K. Maloney and N. Fleck, "Damage tolerance of an architected adhesive joint," *Int. J. Solids Struct.*, vol. 1, no. 0, pp. 1–11, 2017.

[15]   K. Maloney and N. Fleck, "Tear resistance of a square-wave joint: Experiment versus cohesive zone model," *Int. J. Adhes. Adhes.*, vol. 84, pp. 9–17, 2018.

[16]   B. Haghpanah, S. Chiu, and A. Vaziri, "Adhesively bonded lap joints with extreme interface geometry," *Int. J. Adhes. Adhes.*, vol. 48, pp. 130–138, 2014.

[17]   M. C. Corbett, P. A. Sharos, M. Hardiman, and C. T. McCarthy, "Numerical design and multi-objective optimisation of novel adhesively bonded joints employing interlocking surface morphology," *Int. J. Adhes. Adhes.*, vol. 78, pp. 111–120, 2017.

[18]   M. O'Brien, D. J. Mortell, M. C. Corbett, R. M. O'Higgins, and C. T. McCarthy, "Mechanical performance and failure behaviour of miniature aluminium joints with novel interlocking reinforcement," *Int. J. Adhes. Adhes.*, vol. 95, no. August, 2019.

[19]   W. S. Kim, I. H. Yun, J. J. Lee, and H. T. Jung, "Evaluation of mechanical interlock effect on adhesion strength of polymermetal interfaces using micro-patterned surface topography," *Int. J. Adhes. Adhes.*, 2010.

[20]   Y. Hikosaka, R. Matsuzaki, A. Todoroki, and Y. Mizutani, "Enhancement of interfacial fracture toughness of carbon/epoxy composite adhesive joints by in-mold surface preparation," *Express Polym. Lett.*, vol. 7, no. 3, pp. 293–303, 2012.

[21]   R. Matsuzaki, N. Tsukamoto, and J. Taniguchi, "Mechanical interlocking by imprinting of undercut micropatterns for improving adhesive strength of polypropylene," *Int. J. Adhes. Adhes.*, vol. 68, pp. 124–132, 2016.

[22]   "Araldite rapid datasheet: Hunstaman advanced materials," 2011.